Electronic Supplementary Material (ESI) for ChemComm.
This journal is © The Royal Society of Chemistry 2015

Electronic Supporting Information (ESI) for:

Fast lithium-ionic conduction in a new complex hydride–sulphide crystalline phase

Atsushi Unemoto,[a,*] Hui Wu,[b] Terrence J. Udovic,[b] Motoaki Matsuo,[c] Tamio Ikeshoji,[a,c] and Shin-ichi Orimo[a,c]

[a] WPI–Advanced Institute for Materials Research, Tohoku University, Sendai 980-8577, Japan.
[b] NIST Center for Neutron Research, National Institute of Standards and Technology, Gaithersburg, MD 20899-6102, USA
[c] Institute for Materials Research, Tohoku University, Sendai 980-8577, Japan.

*E-mail: unemoto@imr.tohoku.ac.jp

The mention of all commercial suppliers in this paper is for clarity. This does not imply the recommendation or endorsement of these suppliers by NIST.

Preparation of complex hydride–sulfide crystals

A pseudo-ternary system, $LiBH_4$–P_2S_5–Li_2S, was divided into four pseudo-binary systems, namely xLiBH$_4$–(100–x)P$_2$S$_5$ (x = 97.5, 95, 90, 87.5, 85, 80 and 67), yLiBH$_4$–(100–y)Li$_2$S (y = 90, 75 and 50), p(90LiBH$_4$–10P$_2$S$_5$)–(100–p)Li$_2$S (p = 90, 75, 65, 50 and 25) and q(90LiBH$_4$–10P$_2$S$_5$)–(100–q)(90LiBH$_4$–10Li$_2$S) (q = 75, 50 and 25). The powders of $LiBH_4$ (> 95 %, Sigma-Aldrich), P_2S_5 (99 %, Sigma-Aldrich) and Li_2S (99.98 %, Sigma-Aldrich) were used as starting materials. These powders were weighed in desired ratios, and mixed in an agate mortar with an agate pestle, and further mixed via planetary ball-milling (Fritsch, P–7) at a rotation rate of 400 rpm for 5 h with 20 stainless-steel balls having 8-mm-diameter. The resultant powders were annealed at 423 K for 2 h in an Ar-filled environment.

Discussion on crystal structures

The X-ray diffraction (XRD) measurements were carried out for the product powders. The resultant powder after the mechanical ball milling and subsequent annealing was placed into a glass capillary with 0.5 mm inner diameter. The XRD patterns were collected with CuKα radiation (X'pert PRO, PANalytical).

Powder XRD patterns of the pseudo-binary system comprising of $LiBH_4$ and P_2S_5 obtained at room temperature are shown in Fig. S1 (a). Those of the as-received $LiBH_4$ and P_2S_5 are also shown for comparison. Within this pseudo-binary system, only broadened patterns were obtained for $x \leq 80$ in xLiBH$_4$–(100–x)P$_2$S$_5$. Diffraction peaks from a new crystalline phase appeared with increasing x. When x exceeds 95, diffraction peaks owing to unreacted/remaining $LiBH_4$ appeared. The results suggest that the new crystalline phase precipitates in the highest concentration for $85 \leq x \leq 95$. The XRD patterns appearing for 90LiBH$_4$:10P$_2$S$_5$ could be indexed by an orthorhombic system with lattice parameters of a = 5.061 Å, b = 7.149 Å and c = 11.805 Å.

Additional neutron powder diffraction (NPD) measurements using the NIST BT-1 High-Resolution Neutron Powder Diffractometer were carried out at 4 K and 295 K for $90Li^{11}BD_4$:$10P_2S_5$. Here, $Li^{11}BD_4$ (Katchem) was used instead of $LiBH_4$ in the starting materials. The sample was prepared in the same manner as described above.

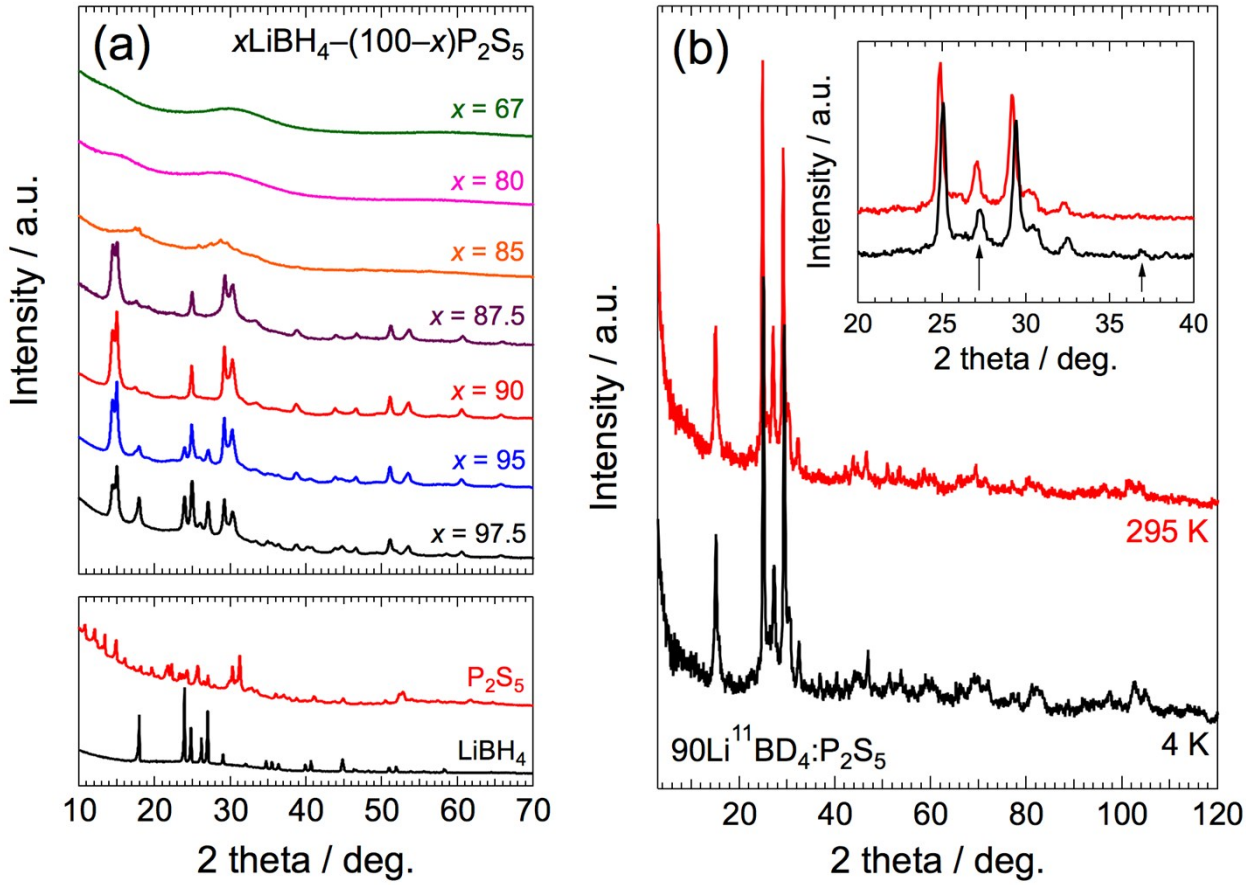

FIGURE S1. (a) Powder XRD patterns of a pseudo-binary system, xLiBH$_4$–(100–x)P$_2$S$_5$ (x = 97.5, 95, 90, 87.5, 85, 80 and 67), obtained at room temperature as a function of x. The as-received P_2S_5 and $LiBH_4$ were also shown for comparison. (b) NPD patterns of $90Li^{11}BD_4$:$10P_2S_5$ obtained at 4 K (black) and 295 K (red). Inset: NPD patterns of $90Li^{11}BD_4$:$10P_2S_5$ in narrower diffraction angle. The arrows represent the diffraction peaks of $Li^{11}BD_4$.

Prompt gamma activation analysis

Since the actual elemental ratios (i.e., chemical formula) of the new crystalline phase in $90LiBH_4$:$10P_2S_5$ are unknown and may be different from those of the starting materials, we decided to estimate the constituent element ratios of the post-ball-milled/annealed materials. Neutron prompt gamma-ray activation analysis (PGAA; a quantitative analysis technique) using the NIST NGD cold-neutron PGAA spectrometer [S1], was employed to determine the elemental ratios in treated $90LiBH_4$:$10P_2S_5$. Here, an additional $90^7Li^{11}BH_4$:$10P_2S_5$ sample was prepared using $^7Li^{11}BH_4$ (Katchem) in the starting materials. From PGAAs of both samples and $^7Li^{11}BH_4$, $LiBH_4$, Li_2SO_4, Li_3PO_4 and Li_2SO_4/Li_3PO_4 mixtures, we were able to obtain estimates of these elemental ratios. Although $90LiBH_4$:$10P_2S_5$ nominally contains Li:B:H:P:S = 90:90:360:20:50, the PGAA-derived ratios were 90:63:204:18:46 (S/P = 2.55(5), H/B = 3.219(3), Li/S = 1.96(2) and Li/B = 1.42(2)). This suggests that B and H were reduced during the synthesis as gaseous species and/or precipitates, and as a result, some or all of the original $[BH_4]^-$ anions in $90LiBH_4$:$10P_2S_5$ no longer

remain intact.

Neutron vibrational spectrometry

To examine what hydrogenous species are present in $90LiBH_4{:}10P_2S_5$, we performed neutron vibrational spectroscopy (NVS) measurements of both $90^7Li^{11}BH_4{:}10P_2S_5$ and $90Li^{11}BD_4{:}10P_2S_5$ using the NIST Filter-Analyzer Neutron Spectrometer [S2]. Due to the overwhelmingly high incoherent neutron scattering cross section for H relative to other elements, NV spectra are dominated by vibrational modes involving H displacements. A comparison of these 4 K NV spectra with those for $LiBH_4$, Li_2BH_4I [S3], NH_3BH_3 [S4], $N_2H_4BH_3$ [S5], and LiH are shown in Fig. S2. The $90Li^{11}BD_4{:}10P_2S_5$ spectrum is a slightly anharmonic energy-downscaled (energy×0.76) version of the $90^7Li^{11}BH_4{:}10P_2S_5$ spectrum due to the doubled mass of D atoms compared to H atoms. It is clear that the $90^7Li^{11}BH_4{:}10P_2S_5$ spectrum does not resemble that for orthorhombic (o) $LiBH_4$, although there are similarities in the B–H bending mode region between 130 meV and 170 meV. The $90^7Li^{11}BH_4{:}10P_2S_5$ spectrum does not have the well-defined $[BH_4]^-$ translational and librational bands of o-$LiBH_4$ near 27 meV and 52 meV (but rather only more broadened features somewhat like for Li_2BH_4I, which is a hexagonal (h) disordered solid-solution of $LiBH_4$ and LiI), and there is an additional B–H bending mode band for the former near 150 meV that is absent for o-$LiBH_4$. Moreover, the $90^7Li^{11}BH_4{:}10P_2S_5$ spectrum possesses an additional non-$[BH_4]^-$-like fundamental band near 100 meV that is also absent for both o-$LiBH_4$ and h-Li_2BH_4I. (N.B., the minor o-$LiBH_4$ bands near 75 and 100 meV are combination and overtone bands due to the sharp fundamental modes at lower energy.) The extra $90^7Li^{11}BH_4{:}10P_2S_5$ features near 100 meV and 150 meV are more reminiscent of rocking and bending modes, respectively, of a $-BH_3$ fragment, as observed for NH_3BH_3 [S4] and $N_2H_4BH_3$ [S5]. Yet, other BH_x fragments or even fragments involving P–H or S–H bonds cannot discounted at this point. In fact, LiH also displays a band near 95 meV, although its higher accompanying 128 meV band is not present in the $90^7Li^{11}BH_4{:}10P_2S_5$ spectrum.

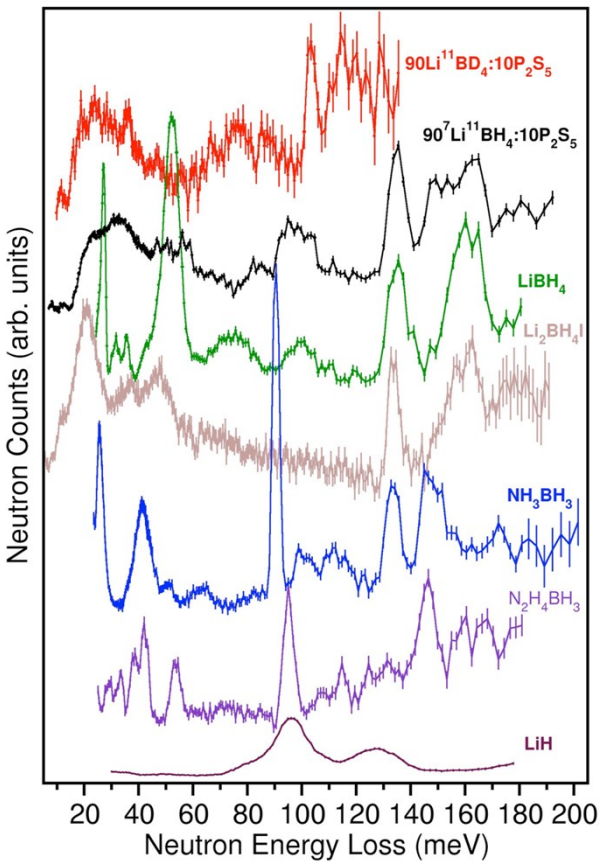

FIGURE S2. Neutron vibrational spectra of $90Li^{11}BD_4:10P_2S_5$, $90^7Li^{11}BH_4:10P_2S_5$, $LiBH_4$, Li_2BH_4I solid solution [S3], NH_3BH_3 [S4], $N_2H_4BH_3$ [S5], and LiH obtained at 4 K.

Quasi-elastic neutron scattering

Quasielastic neutron scattering measurements on $90^7Li^{11}BH_4:10P_2S_5$ and $^7Li^{11}BH_4$ were carried out using the NIST High-Flux Backscattering Spectrometer [S6] for the fixed-window scans (FWSs) shown in Fig. 2 of the paper, and the NIST Disk Chopper Spectrometer (DCS) [S7] for complementary quasielastic spectra (as exemplified in the Fig. 2 inset). The QENS data were treated with the DAVE software package [S8]. The comparison of the FWSs for $90^7Li^{11}BH_4$ in Fig. 2 indicate an earlier onset for H mobility for $90^7Li^{11}BH_4:10P_2S_5$ (at ~80 K) compared to that for $^7Li^{11}BH_4$ (at ~160 K). Also, the decreasing FWS slope is more gradual for $90^7Li^{11}BH_4:10P_2S_5$, suggesting a smaller activation energy for H jump reorientations than for $^7Li^{11}BH_4$ and/or a distribution of H mobilities.

We found that the DCS QENS spectra for $90^7Li^{11}BH_4:10P_2S_5$, were better fit with two different Lorentzian components along with the expected additional delta function, all convoluted with the instrumental resolution function measured below 50 K. Figure S3 illustrates the resulting elastic incoherent structure factor (EISF) dependence on momentum transfer Q for $90^7Li^{11}BH_4:10P_2S_5$ at both 300 and 325 K assuming two Lorentzian components (with Lorentzian fwhm widths of 0.13 and 0.84 meV at 300 K and 0.20 and 1.67 meV at 325 K), The shape and position of the EISF minimum suggests a single H-H jump distance of ~2 Å, consistent with the H-H distances associated with both $[BH_4]^-$ anions and $–BH_3$ fragments. The data fit within an EISF band that is consistent with one-fourth to one-third of the H atoms in the material remaining immobile (such as in $=BH_2$, $≡BH_3$, –SH, –PH, or LiH species) while the rest undergo 3-fold (such as for $–BH_3$) and/or tetrahedral tumbling motions (such as for $[BH_4]^-$ anions). We will have a much clearer picture of the H dynamics after the unknown crystal structure is finally determined.

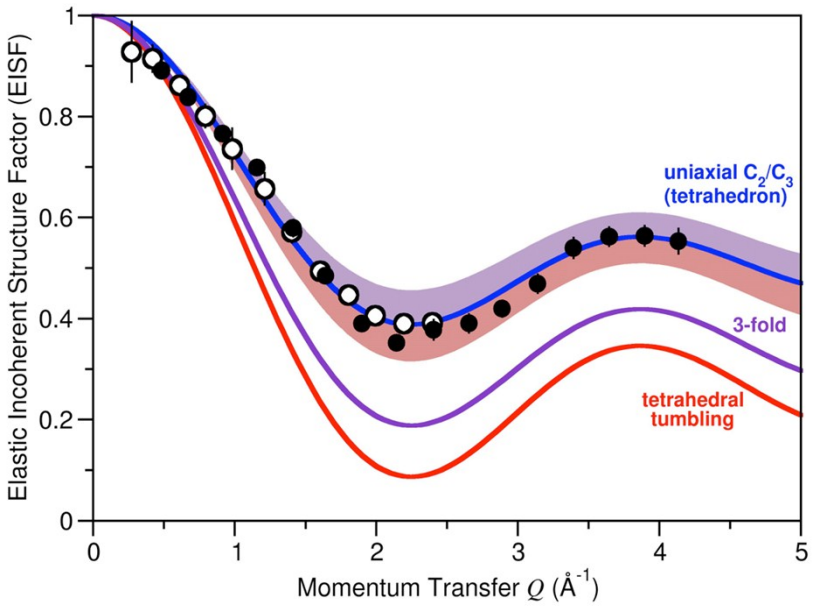

FIGURE S3. Elastic incoherent structure factor (EISF) vs. momentum transfer Q for $90^7Li^{11}BH_4:10P_2S_5$ assumed two Lorentzian components: at 300 K for 4.8 Å neutrons (56 μeV fwhm resolution; open circles) and at 325 K for 2.75 Å neutrons (275 μeV fwhm resolution; closed circles). Red, purple, and blue curves denote three respective H jump models, assuming a H-H jump distance of 2 Å: tumbling of H among four-corners of a tetrahedron (such as for $[BH_4]^-$), 3-fold uniaxial reorientation (such as for $–BH_3$), and uniaxial C_2 or C_3 reorientations of H in a tetrahedral

configuration (such as for $[BH_4]^-$). (N.B., the latter model is indistinguishable to that for 3-fold – BH_3 jumps with an additional immobile H atom present). The mauve and pink bands encompass the swath of EISF models where one-fourth to one-third of the H atoms present in the material remain immobile while the rest undergo 3-fold (mauve EISF band) and/or tetrahedral tumbling motions (pink EISF band).

Differential scanning calorimetry

Differential scanning calorimetry (DSC) was carried out for the as-ball milled $90LiBH_4$ + $10P_2S_5$ (without heating) and the as-synthesized powders at a heating rate of 5 K min^{-1} for two temperature cycles. A reference Al_2O_3 powder and an Al pan were used for the measurements. During measurements, the temperature was kept at 473 K for 1 h after the samples reached this temperature. During the initial heating run of the as-ball-milled $90LiBH_4$ + $10P_2S_5$, distinct endothermic peaks appeared at 332, 379 and 428 K while exothermic peaks appeared at 341 and 389 K, as shown in Fig. S4 (a). No peaks were observed during the 1st cooling and subsequent 2nd heating and cooling runs. The DSC profiles of the as-synthesized $90LiBH_4$:$10P_2S_5$ do not have any remarkable peaks during the temperature scan, as shown in Fig. S4 (b). The results suggest that the peaks appearing for the mixed $LiBH_4$ and P_2S_5 powder arise mainly from the formation process of a new crystalline phase in $90LiBH_4$:$10P_2S_5$. The annealing at 423 K for 2 h in an Ar atmosphere, which we also employed for the synthesis, is sufficient to complete the formation reaction of $90LiBH_4$:$10P_2S_5$. $90LiBH_4$:$10P_2S_5$ does not undergo a phase transition within the temperature range of the DSC measurement, contrary to $LiBH_4$ [S9]. This means that unreacted/remaining $LiBH_4$ in $90LiBH_4$:$10P_2S_5$ is negligibly small, and is consistent with the result of the conductivity measurement that a visible conductivity jump did not occur over the temperature range investigated, as shown in Figs. 1 and S5.

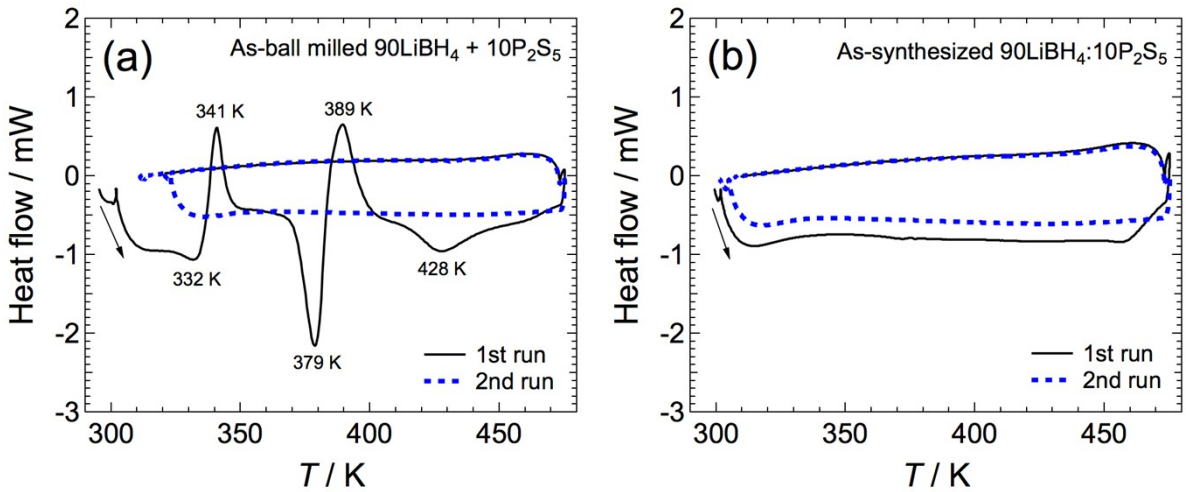

FIGURE S4. DSC profiles of (a) the as-milled $90LiBH_4$ + $10P_2S_5$ and (b) the as-synthesized $90LiBH_4$:$10P_2S_5$ at a heating rate of 5 K min^{-1} in the temperature range from room temperature to 473 K. The temperature was kept for 1 h when reached at 473 K. Black and blue curves show the initial and the second temperature cycles, respectively.

Conductivity and cyclic voltammetry measurements

The compacts of the products were prepared for the conductivity measurements by the two-probe ac technique. The synthesized powders were placed in an 8-mm-diameter die and then

uniaxially pressed at 240–180 MPa. The resultant compacts were sandwiched by Li electrodes, and placed in a stainless-steel electrochemical cell, as schematically illustrated elsewhere [S10]. The electrochemical cell was connected to a Chemical Impedance Meter (3532–80, Hioki Corp.). The input voltage perturbation and the frequency range were 100 mV and 1 M–4 Hz, respectively. The ac impedance measurements were carried out by temperature cycles from room temperature to 423 K with 10 K step intervals.

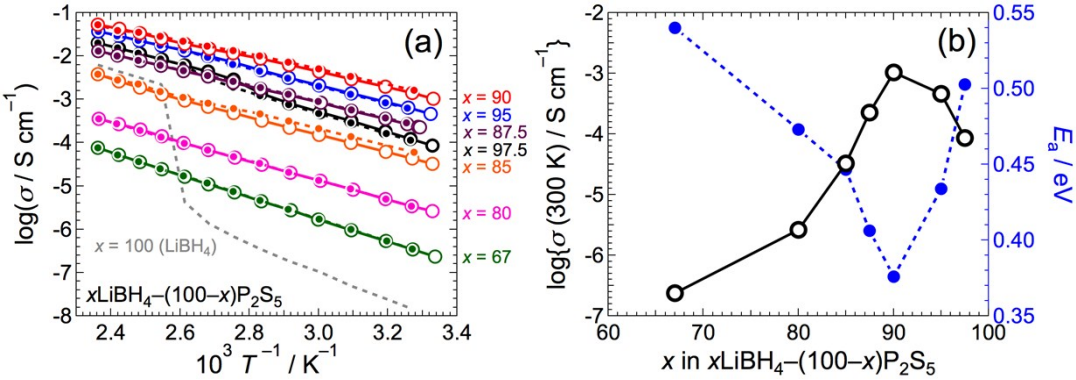

FIGURE S5. (a) Electrical conductivity of the pseudo-binary system, xLiBH$_4$–(100–x)P$_2$S$_5$ (x = 100 [S9], 97.5, 95, 90, 87.5, 85, 80 and 67), as a function of inverse temperature. (b) The ionic conductivity at 300 K, and the activation energies of xLiBH$_4$–(100–x)P$_2$S$_5$ as a function of x. Closed and open symbols show the conductivities obtained during heating and cooling runs, respectively.

Figure S5 (a) shows electrical conductivities of xLiBH$_4$–(100–x)P$_2$S$_5$ (x = 100 [S9] and 97.5–67) as a function of inverse temperature. The electrical conductivities increased monotonically with increasing x for $x \leq 90$, while they decreased with increasing x for $x \geq 90$. The electrical conductivity at 300 K and the activation energies are shown in Fig. S5 (b). The electrical conductivity and the activation energy were the largest and the lowest for x = 90. These are log{σ (300 K) / S cm^{-1}} = –3.0 and 0.38 eV, respectively. Considering the results together with the XRD measurements (Fig. S1 (a)), the fast lithium-ionic conducting crystalline phase precipitates in the highest concentration for x = 90. For $x \geq 95$, conductivity hysteresis is observed around the phase transition temperature of LiBH$_4$, i.e. 390 K [S9]. This suggests that remaining LiBH$_4$ in xLiBH$_4$–(100–x)P$_2$S$_5$ also contributed to the conductivity at temperatures higher than that temperature. This is consistent with the results of the XRD measurements.

The partial conductivity contributions, i.e. lithium-ionic and electronic conductivities, were evaluated by means of a dc technique using the following electrochemical cells with the 90LiBH$_4$:10P$_2$S$_5$ electrolyte at 300 K:

Cell–1; Li | Li$_4$(BH$_4$)$_3$I | 90LiBH$_4$:10P$_2$S$_5$ | Li$_4$(BH$_4$)$_3$I | Li
Cell–2; Stainless-steel (SS) | 90LiBH$_4$:10P$_2$S$_5$ | SS

where 30 mg of 90LiBH$_4$:10P$_2$S$_5$ was used for the electrolyte layer. For the Cell–1, 20 mg of Li$_4$(BH$_4$)$_3$I was placed between the lithium electrode and 90LiBH$_4$:10P$_2$S$_5$ electrolyte. Since Li$_4$(BH$_4$)$_3$I is a pure lithium-ionic conductor [S11], and it thus forms a blocking interface for electronic species. When a steady-state current is observed under a constant dc voltage, it represents the contribution of lithium-ionic current. On the other hand, the SS electrode forms a blocking interface for lithium-ions with the electrolyte, and thereby a steady-state current signifies to the

transport of electrons. Both experimental results thus enable us to evaluate the partial conductivity contributions of lithium-ions and electrons for $90LiBH_4{:}10P_2S_5$.

Figure S6 shows current relaxation curves for Cell–1 and –2 under a constant dc voltage as a function of time. For the Cell–1, a steady-state current of $\log(i\ /\ \mu A\ cm^{-2}) = 1.0$ was observed when a 50 mV dc voltage was applied. On the other hand, the observed logs of the currents were on the order of –2, and those were independent of the dc voltage for the Cell–2. This implies that the available current passing through the $90LiBH_4{:}10P_2S_5$ electrolyte with the SS electrodes is less than the detection limit of the electro-analytical system used. The contribution of electronic current is negligibly small, and thereby $90LiBH_4{:}10P_2S_5$ is considered a pure lithium-ionic conductor.

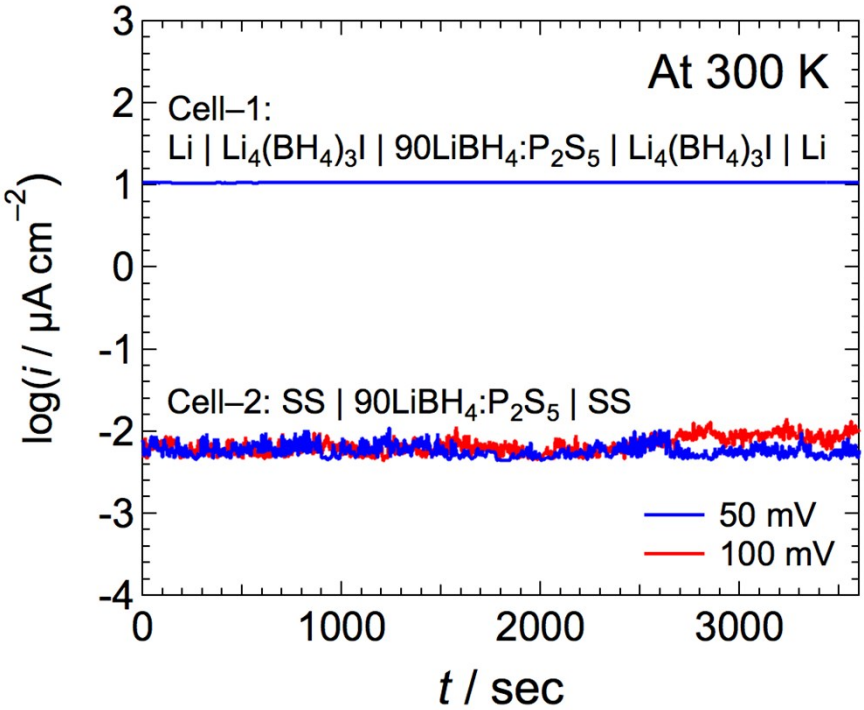

FIGURE S6. Current relaxation curves under a constant voltage of the Li | $Li_4(BH_4)_3I$ | $90LiBH_4{:}10P_2S_5$ | $Li_4(BH_4)_3I$ | Li (Cell–1) and the SS | $90LiBH_4{:}10P_2S_5$ | SS (Cell–2) cells obtained at 300 K.

Figure S7 (a), (b) and (c) show the electrical conductivities of pseudo-binary systems, yLiBH$_4$–(100–y)Li$_2$S (y = 90, 75 and 50), p(90LiBH$_4$–10P$_2$S$_5$)–(100–p)Li$_2$S (p = 90, 75, 65, 50 and 25) and q(90LiBH$_4$–10P$_2$S$_5$)–(100–q)(90LiBH$_4$–10Li$_2$S) (q = 75, 50 and 25), respectively. For yLiBH$_4$–(100–y)Li$_2$S, conductivity jumps around the phase transition temperature of LiBH$_4$ were observed regardless of y. This means that any phase that possesses fast lithium-ionic conductivity is not included in this pseudo-binary system with a LiBH$_4$-rich region. For p(90LiBH$_4$–10P$_2$S$_5$)–(100–p)Li$_2$S and q(90LiBH$_4$–10P$_2$S$_5$)–(100–q)(90LiBH$_4$–10Li$_2$S),

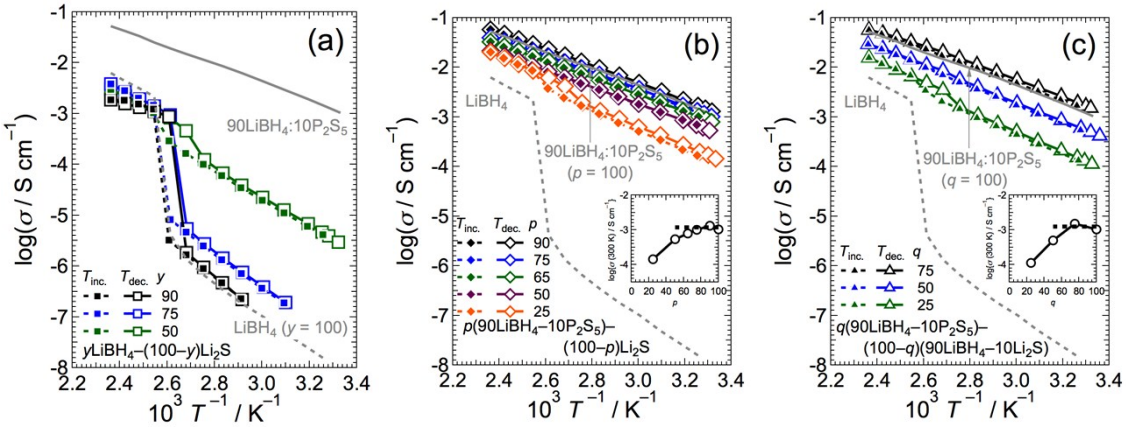

FIGURE S7. Electrical conductivities of pseudo-binary systems, (a) yLiBH$_4$–(100–y)Li$_2$S (y = 90, 75 and 50), (b) p(90LiBH$_4$–10P$_2$S$_5$)–(100–p)Li$_2$S (p = 90, 75, 65, 50 and 25) and (c) q(90LiBH$_4$–10P$_2$S$_5$)–(100–q)(90LiBH$_4$–10Li$_2$S) (q = 75, 50 and 25) as a function of inverse temperature. The insets in (b) and (c) show the electrical conductivities at 300 K, log{σ (300 K) / S cm^{-1}}, as functions of p and q, respectively. Closed and open symbols show the conductivities obtained during heating and cooling runs, respectively. Insets in (b) and (c): log{σ (300 K) / S cm^{-1}} as functions of p and q, respectively.

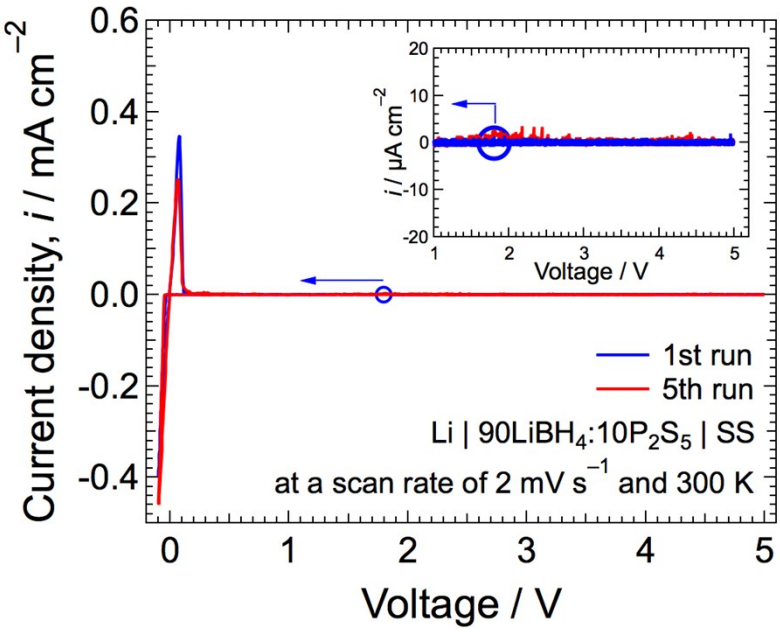

FIGURE S8. Cyclic voltammogram of the asymmetric Li | 90LiBH$_4$:10P$_2$S$_5$ | stainless-steel (SS) cell operated at 300 K and a 2 mV s^{-1} sweep rate with 5 cycles. The inset shows the profiles representing the higher voltage range with a μA cm^{-2} scale for the vertical axis. The initial run started from the open blue circle toward low voltage.

conductivities became close to that of 90LiBH$_4$:10P$_2$S$_5$ with increasing p and q. The fast lithium-ionic conduction phase is thus included only for 90LiBH$_4$:10P$_2$S$_5$. Note that there were no clear indications of the existence of another crystalline phase except for LiBH$_4$, Li$_2$S and 90LiBH$_4$:10P$_2$S$_5$ in the XRD patterns (data not shown). The results suggest that no other new crystalline phase is included in the system by means of our synthetic route employed in this study.

The results of XRD and conductivity measurements tell us that the concentration of the

new crystalline phase becomes highest for $x = 90$ in xLiBH$_4$–(100–x)P$_2$S$_5$, namely 90LiBH$_4$:10P$_2$S$_5$, in the products. Thus, the 90LiBH$_4$:10P$_2$S$_5$ electrolyte was subjected to an electrochemical potential window analysis by a cyclic voltammetry (CV) measurement. The 90LiBH$_4$:10P$_2$S$_5$ electrolyte was sandwiched by Li and SS electrodes. The resultant asymmetric cell was connected to VersaSTAT4 (Princeton Applied Research). The measurement was carried out at 300 K and a 2 mV s^{-1} sweep rate in the voltage range from –0.1 to 5 V, and the result is shown in Fig. S8. In the cyclic voltammogram, reversible lithium dissolution/striping was observed nearly at 0 V, and no irreversible oxidation current appeared up to 5 V in the CV profiles. The results imply that the 90LiBH$_4$:10P$_2$S$_5$ electrolyte has a wide potential window, and thereby promises repeated operation of the bulk-type all-solid-state battery.

Battery test

TiS$_2$ (99.9 %, Sigma-Aldrich) and Li foil (Honjo Metal Co., Ltd.) were used as a positive electrode active material and negative electrode, respectively. The TiS$_2$ and as-synthesized 90LiBH$_4$:10P$_2$S$_5$ powders were weighed in a 2:3 mass ratio, and mixed by an agate mortar in an agate pestle. The resultant powder was used for the composite positive electrode. We assembled here the bulk-type all-solid-state batteries with the following configurations:

Battery–A; TiS$_2$/90LiBH$_4$:10P$_2$S$_5$ | 90LiBH$_4$:10P$_2$S$_5$ | InLi (discharge–charge profiles appearing in the main body of the manuscript, Fig. 3)

Battery–B; TiS$_2$/90LiBH$_4$:10P$_2$S$_5$ | 90LiBH$_4$:10P$_2$S$_5$ | Li$_4$(BH$_4$)$_3$I | Li

For the battery–A assembly, 6 mg of the composite positive electrode, 25 mg of the 90LiBH$_4$:10P$_2$S$_5$ electrolyte (500 μm thickness) were transferred in an 8-mm-diameter die, and uniaxially pressed at 240 MPa. The 10-mm-diameter In and Li foils (200 μm and 17 μm thicknesses, respectively) were placed in this order on the opposite of the positive electrode layer. The resultant battery was annealed at 343 K for 12 h for a negative electrode alloying, and subsequently temperature was decreased down to 300 K for the battery test. Prior to the battery–B assembly, Li$_4$(BH$_4$)$_3$I was synthesized via the mechanical ball milling at 400 rpm for 5 h in Ar environment, and then used as an interlayer between the electrolyte and the lithium negative electrode. 6 mg of the composite positive electrode, 20 mg of the 90LiBH$_4$:10P$_2$S$_5$ and 5 mg of the Li$_4$(BH$_4$)$_3$I were transferred in this order in an 8-mm-diameter die, and uniaxially pressed at 240 MPa (thickness was estimated to be approximately 100 μm for the composite positive electrode, 400 μm for the electrolyte and 70 μm for the interlayer). The Li foil was placed opposite of the positive electrode layer.

The assembled bulk-type all-solid-state TiS$_2$/InLi and TiS$_2$/Li batteries (the battery–A and –B, respectively) was transferred into a stainless steel electrochemical cell with a Teflon® guide. Microstructure and element distributions of the composite positive electrode were analyzed by a scanning electron microscope (SEM, JSM-6009, JEOL Ltd.) equipped with an energy dispersive X-ray spectrometer (EDS, EX-54175JMH, JEOL Ltd.). The assembled battery was connected to a 580 Battery Test System (Scribner Associates Inc.), and the battery tests were carried out with 0.1 C charge rate (114 μA cm^{-2}) in the voltage range of 0.9–2.3 V for battery–A, and 0.05 C (57 μA cm^{-2}) in 1.6–2.7 V for the battery–B at 300 K.

Highly deformable 90LiBH$_4$:10P$_2$S$_5$ new phase allows for inducing the extensive

interfacial contact between TiS_2 and $90LiBH_4:10P_2S_5$ phases in the composite positive electrode layer merely by a uniaxial pressing at 240 MPa and room temperature, as shown by the microstructure and element distributions in Fig. S9. Such a robust interface facilitates a smooth charge transfer reaction between the two phases, and thereby allowed a repeated operation of the bulk-type all-solid-state batteries at 300 K, as shown in Fig. 3 and Fig. S11.

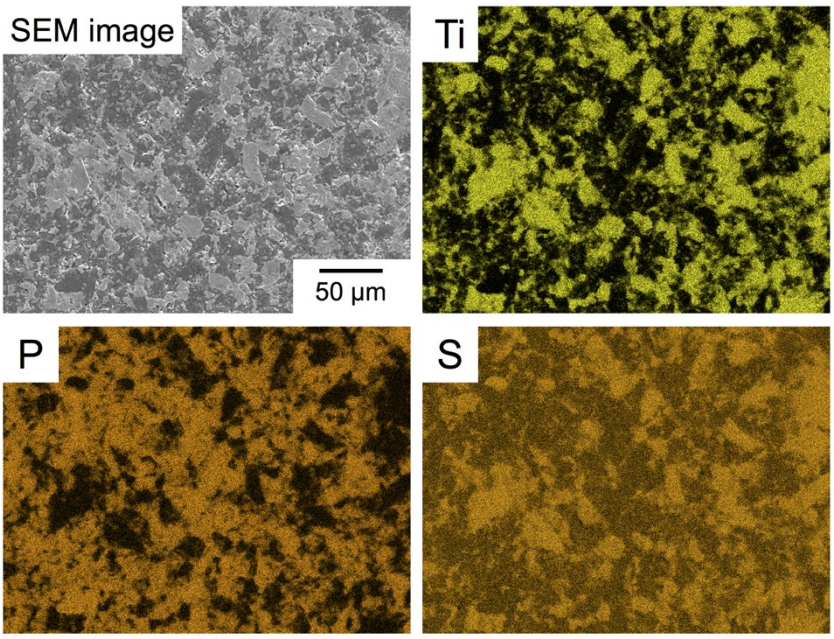

FIGURE S9. SEM image and distributions of Ti, P and S of the surface of the composite positive electrode consisting of TiS_2 and $90LiBH_4:10P_2S_5$.

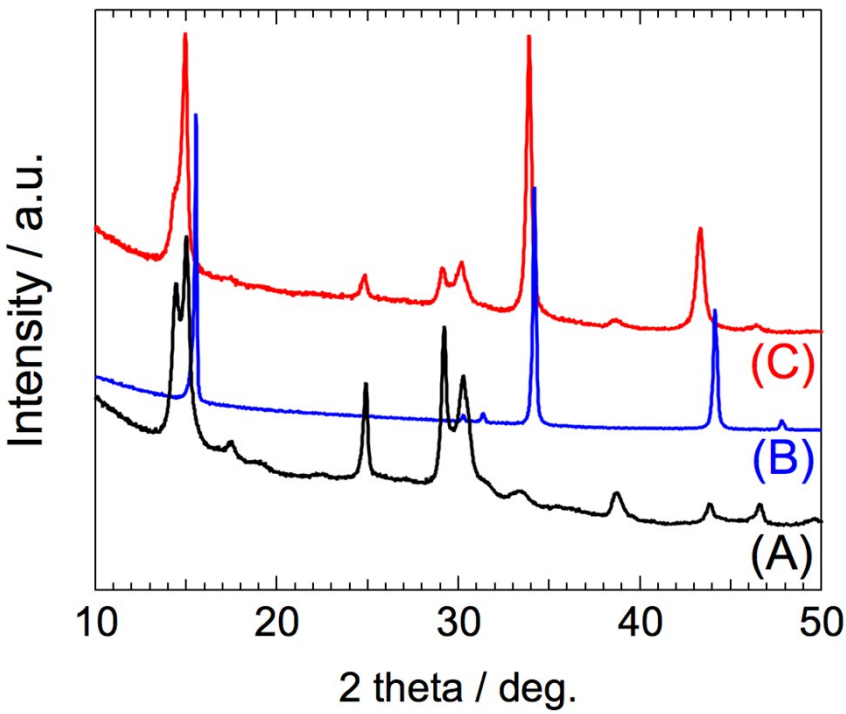

FUGURE S10. Powder XRD pattenrs of (A) the as-prepared $90LiBH_4:10P_2S_5$, (B) the as-received TiS_2 and (C) the $TiS_2/90LiBH_4:10P_2S_5$ mixture as a result of annealing at 343 K for 12 h in Ar environment.

Repeated discharge–charge operation of the battery–A could be successfully realized with a high TiS_2 utilization ratio (239 mAh g^{-1} in theoretical capacity [S12, S13]), as shown in Fig. 3 (main body of the manuscript). Our battery exhibited the initial and second discharge capacities of 192 and 228 mAh g^{-1}, respectively, at the battery operating temperature of 300 K and 0.1 C. Low initial discharge capacity of the battery–A (Fig. 3) is related to the solid-state reaction between TiS_2 and $90LiBH_4$:$10P_2S_5$ during LiIn alloying at 343 K for 12 h before the battery test. To confirm this, we carried out powder XRD measurements on the as-prepared $90LiBH_4$:$10P_2S_5$, as-received TiS_2 and the TiS_2/$90LiBH_4$:$10P_2S_5$ mixture after annealing at 343 K for 12 h in Ar environment at room temperature, and the results are shown in Fig. S10. The as-received TiS_2 had the lattice parameters of a = 3.4061(2) Å and c = 5.6986(7) Å (space group: P–3m1). These are consistent with those reported in the preceding papers [S14, S15]. As a result of annealing of the TiS_2 and $90LiBH_4$:$10P_2S_5$ mixture at 343 K for 12 h in Ar environment, the TiS_2 diffraction peaks shifted to lower angle. This means that lattice expansion of TiS_2 occurred as a result of annealing. From the relationship between the lattice parameters and the lithium concentration in Li_xTiS_2 [S14], the lithium concentration in the mixture could be estimated under the assumption that the lattice expansion is caused only by the lithium intercalation into TiS_2. It was less than 15 mol % ($Li_{0.15}TiS_2$), corresponding to a specific capacity of 35 mAh g^{-1}. This value is almost equal to the difference between the theoretical capacity and the initial discharge capacity. Considering this, both the smaller initial discharge capacity compared to the second one and the shift of discharge profiles toward lower voltage are reflective of a solid-state reaction (i.e., self-discharge) between TiS_2 and $90LiBH_4$:$10P_2S_5$ during LiIn alloying.

The self-discharge reaction seen in the battery–A is hindered when the battery is not exposed to higher temperatures. To confirm this, we assembled the battery–B that allows for using the lithium negative electrode and does not require annealing before the battery test. Figure S11 shows the 1st–3rd discharge–charge profiles of the bulk-type all-solid-state TiS_2/Li battery (battery–B) using the $90LiBH_4$:$10P_2S_5$ electrolyte operated at 300 K and 0.05 C (57 μA cm^{-2}). We placed the interlayer, $Li_4(BH_4)_3I$, for the inhibition of the reaction between the $90LiBH_4$:$10P_2S_5$ electrolyte and Li negative electrode during charging. This issue is also

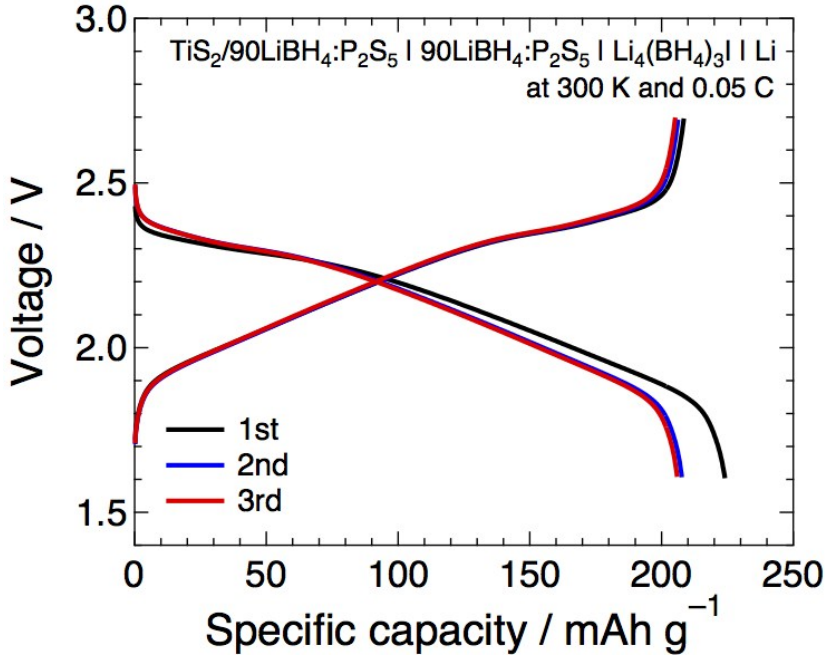

FIGURE S11. Discharge–charge profiles of the bulk-type all-solid-state TiS_2/Li battery (battery–B)

using the $90LiBH_4$:$10P_2S_5$ electrolyte operated at 300 K and 0.05 C (57 μA cm^{-2}).

overcome by employing the InLi alloy negative electrode as the discharge–charge profiles indicate in the main body of the manuscript, Fig. 3 (battery–A). TiS_2 has a theoretical capacity of 239 mAh g^{-1} [S12, S13]. Our battery exhibited the initial discharge and charge capacities of 224 and 208 mAh g^{-1}, respectively, and coulombic efficiency was as high as 93 %. The reversible specific capacities of nearly 205 mAh g^{-1} were achieved over the battery test.

REFERENCES

[S1] R. L. Paul, D. Sahin, J. C. Cook, C. Brocker, R. M. Lindstrom, D. J. O'Kelly, *J. Radioanal. Nucl. Chem.* 304 (2015) 189.
[S2] T. J. Udovic, C. M. Brown, J. B. Leão, P. C. Brand, R. D. Jiggetts, R. Zeitoun, T. A. Pierce, I. Peral, J. R. D. Copley, Q. Huang, D. A. Neumann, R. J. Fields, *Nucl. Instr. And Meth. A* 588 (2008) 406.
[S3] N. Verdal, T. J. Udovic, J. J. Rush, H. Wu, A. V. Skripov, *J. Phys. Chem. C* 117 (2013) 12010.
[S4] S. Gadipelli, J. Ford, W. Zhou, H. Wu, T. J. Udovic, T. Yildirim, *Chem. Eur. J.* 17 (2011) 6043.
[S5] Y. S. Chua, Q. Pei, X. Ju, W. Zhou, T. J. Udovic, G. Wu, Z. Xiong, P. Chen, H. Wu, *J. Phys. Chem. C* 118 (2014) 11344.
[S6] A. Meyer, R. M. Dimeo, P. M. Gehring, D. A. Neumann, *Rev. Sci. Instrum.* 74 (2003) 2759.
[S7] J. R. D. Copley, J. C. Cook, *Chem. Phys.* 292 (2003) 477.
[S8] R. T. Azuah, L. R. Kneller, Y. Qiu, P. L. W. Tregenna-Piggott, C. M. Brown, J. R. D. Copley, R. M. Dimeo, *J. Res. Natl. Inst. Stan.* 114 (2009) 341.
[S9] M. Matsuo, Y. Nakamori, S. Orimo, H. Maekawa, H. Takamura, *Appl. Phys. Lett.* 91 (2007) 224103.
[S10] A. Unemoto, S. Yasaku, G. Nogami, M. Tazawa, M. Taniguchi, M. Matsuo, T. Ikeshoji, S. Orimo, *Appl. Phys. Lett.* 105 (2014) 083901.
[S11] H. Maekawa, M. Matsuo, H. Takamura, M. Ando, Y. Noda, T. Karahashi, S. Orimo, *J. Am. Chem. Soc.* **131** (2009) 894.
[S12] M. S. Whittingham, *Science* 192 (1976) 1126.
[S13] M. S. Whittingham, *Prog. Solid State Chem.* 12 (1978) 41.
[S14] J. Dahn, W. McKinnon, R. R. Haering, W. Buyers, B. Powell, *Can. J. Phys.* 58 (1980) 207.
[S15] J. Dahn, R. R. Haering, *Solid State Commun.* 40 (1981) 245.